DISPLACEMENT INTERPOLATION USING MONOTONE REARRANGEMENT

DONSUB RIM* AND KYLE T. MANDLI*

Abstract. When approximating a function that depends on a parameter, one encounters many practical examples where linear interpolation or linear approximation with respect to the parameters prove ineffective. This is particularly true for responses from hyperbolic partial differential equations (PDEs) where linear, low-dimensional bases are difficult to construct. We propose the use of *displacement interpolation* where the interpolation is done on the optimal transport map between the functions at nearby parameters, to achieve an effective dimensionality reduction of hyperbolic phenomena. We further propose a multi-dimensional extension by using the intertwining property of the Radon transform. This extension is a generalization of the addedclassical translational representation of Lax-Philips [Lax and Philips, *Bull. Amer. Math. Soc.* 70 (1964), pp.130–142].

1. Introduction. Linear interpolation or linear approximation is a concept that is ubiquitous in computational mathematics. Perhaps the most familiar setting is where one approximates an arbitrary function by a linear sum of functions from a carefully chosen basis $\mathcal{V}$. For example, the basis can be chosen as the Fourier basis, Wavelet basis, or Chebyshev polynomial basis, depending on the application at hand [42, 43, 50, 10]. The approximation with respect to these well-studied bases are guaranteed to be optimal in some sense, often meaning that the number of terms in the linear sum that achieves a desired accuracy is small. Put in other terms, an accurate approximation is presumed to belong to some low-dimensional subspace of the chosen basis $\mathcal{V}$.

A more challenging problem arises when the function to be approximated depends on a parameter. For one fixed parameter value a linear approximation may indeed be optimal, accurately representing the approximand with a few members of $\mathcal{V}$, but a different set of members may be needed for a good approximation at a different parameter value. In the worst case, one would need a large subset of $\mathcal{V}$ to accurately approximate the function over all parameter values, and a low-dimensional representation would be possible only locally. Mathematically speaking, we are describing the situation where the Kolmogorov N-width decays slowly (e.g. linearly) with respect to the dimension N of the basis $\mathcal{V}$ [20]. Unfortunately, this is not a rare worst-case scenario, but is the typical behavior for functions of interest in modeling wave propagation: often the energy of the wave is concentrated at different spatial locations for different parameter values, so that finding a global representation of the wave profile using a fixed low-dimensional subspace is not possible [40, 1, 34, 46]. This high-dimensional nature of wave phenomena can also be characterized terms of the separability of the Green's function for the Helmholtz equation [15], however this difficulty arises even for the simplest of examples [39].

Naturally, this also has important implications for the field of uncertainty quantification (UQ). Many numerical numerical methods devised for propagating uncertainties rely on exploiting some low-dimensional linear subspace for the random parameters. As a prime example, generalized polynomial chaos (gPC) expansions use polynomial bases to efficiently compute the statistics of some quantity of interest (QoI) [48]. However, the slow decay of the Kolmogorov N-width with respect to the uncertain parameters also implies slow convergence of the expansion [47]. A

*Department of Applied Physics and Applied Mathematics, Columbia University, New York, NY 10027 (dr2965@columbia.edu, kyle.mandli@columbia.edu).

closely related subject is that of reduced order models (ROMs) [20, 30]. Once a ROM of a parametrized system is constructed, even naïve Monte Carlo sampling of the full solution becomes feasible. This makes ROMs valuable in various UQ problems, whenever they could be constructed. Nonetheless, projection-based model reduction methods suffer from precisely the same issue pointed out above, due to the lack of a low-dimensional linear basis.

In this paper, we adopt an alternative approach in which we compute the transport map between functions in order to find a low-dimensional structure in the transport maps themselves. Given two wave profiles, we will find the map that will transport each unit mass in the first profile in the most optimal manner to the second profile. This is precisely an optimal transport problem, and the interpolation we are proposing is referred to as *displacement interpolation* in the optimal transport literature [26, 44, 45].

For our purposes, this transport map is found by using the simplest solution to the Monge-Kantorovich optimal transport problem [22, 4] in a single spatial dimension (1D), called *monotone rearrangement*. The problem minimizes the so-called Wasserstein metric between two probability distributions [14], and we will show that a very simple computation will produce the minimizing transport map. Moreover, although the optimal transport problem poses that the two profiles have to be non-negative, this restriction is easily removed by implementing an integral formulation (2.6) rather than a differential formulation (2.7) of the problem. We also extend the computation of transport maps to apply to functions of arbitrary sign. While this may be satisfactory in 1D, wave propagation takes on a much more complicated form in multiple spatial dimensions. We extend our displacement interpolation procedure in 1D to multiple dimensions via a dimensional splitting that exploits the intertwining property of the Radon transform [23, 19, 35]. That is, instead of dealing with the multi-dimensional problem directly, we solve a collection of 1D Monge-Kantorovich problems. This a natural extension of the translational representation of the solution to the wave equation by Lax and Philips [23]. As a result of this interpolation procedure, one discovers a smooth map that interpolates between two wave profiles, even though the profiles themselves can be nearly orthogonal to each other.

Individual components that form the interpolation techniques proposed in this paper are closely related to recent works that have arisen in various contexts. The subject matter spans different fields and its literature is growing rapidly, so we will only provide a limited overview here.

Model reduction. The idea of finding a low-dimensional structure by applying dimensionality reduction in transport maps was also proposed in [21], and these low-rank transport modes were called *advection modes*. Nonetheless, the work suggested using linear programming to compute the optimal transport map in place of the explicit monotone rearrangement, and the multi-dimensional extension was also done by solving an equivalent multi-dimensional optimal transport problem. This incurs a high computational cost, and prohibits its use in practical PDE applications. We note that the authors adapted the interpolation techniques here to build a ROM for paramterized scalar conservation laws [38], motivated by an elegant relationship between optimal transport and scalar conservation laws observed in [5].

Image Processing. Displacement interpolants, or more generally Wasserstein barycenters [2], are useful in image processing for tasks such as shape interpolation, warping, color transfer or texture mixing. In these applications, the Wasserstein metric is commonly used along with an optimization procedure but again, the computational cost was too high [7]. In an effort to find cheaper approximations, both the

monotone rearrangement [13], as well as an approximation to the Wasserstein metric called the *sliced Wasserstein distance* were considered in [33], and the combination of using monotone rearrangement along with the Radon transform was also proposed as an approximation to the sliced Wasserstein barycenters themselves [31, 6]. Remarkably, the transform was proposed chiefly as a way to reduce computational cost and the articles report appearance of artifacts when Radon transforms were used to interpolate between images, which is not unexpected since the most natural interpolants between common images tend to be closer to the motion of a rigid body rather than that of waves. The link between the Radon transforms and hyperbolic PDEs through the intertwining property (2.31) was not made, and the interpolant with artifacts may in fact be the *correct* interpolant we seek for our purposes. On the other hand, breakthroughs in reducing computational costs of the optimal transport problem via entropic-regularization [9, 3] has significantly alleviated the computational burden, so direct computations on the multi-dimensional optimal transport problem appears to be the more desired approach for this class of applications [41].

Wasserstein metric as a misfit function. The Wasserstein metric itself is of great interest apart from our application for interpolation or dimensionality reduction. Also called the *Mallows distance* [25], it has long been studied in the statistics literature in relation to goodness-of-fit tests for non-normality or as measures of similarity between histograms [12, 11, 27], due to its robustness with respect to location-scale families of probability distributions. More recently, the metric has been employed as a misfit function in various applications. For example, it was used in seismic inverse problems [49, 28] to overcome common problems such as cycle-skipping that entails the use of the usual ℓ^2 misfit function. Its application is also being explored in machine learning, for instance as the loss function in supervised learning [16].

Our main contribution is in the generalization of the classical translational representation of Lax-Philips by combining monotone rearrangement with the Radon transform, further extending the approach in conjunction with more general transforms, and applying them for dimensionality reduction of problems involving wave propagation exhibiting high-dimensional behavior. The paper is organized as follows. The displacement interpolant is derived in section 2 through the integral formulation (2.6) of the monotone rearrangement problem. The simplest case of interpolating between two strictly positive 1D profiles is considered first, then restrictions on the signs are gradually removed. Then, a multi-dimensional extension is defined through the Radon transform. Details on numerical implementation and numerical examples illustrating various aspects of the interpolation scheme are presented in section 3.

2. Displacement interpolation. The most common approach to approximating a paramterized function is to apply the method of separation of variables and then to perform linear approximation. Once the parameter function is separated, one chooses a suitable linear basis, then proceeds to find a linear combination of its members that approximates this function.

To make this more explicit, suppose that u is a function that depends on a a vector of parameters $\boldsymbol{\alpha}$, and that we have evaluated the function at various parameter values $\boldsymbol{\alpha}_1, ..., \boldsymbol{\alpha}_N$. That is, we have obtained the set of functions

$$\mathcal{U} = \{u_n = u(\boldsymbol{\alpha}_n) : n = 1, 2, ...N\}.$$

The goal is to interpolate these function with respect to the parameters.

Throughout this paper, we will refer to each member in $\mathcal{U}$ itself as a function, and when referring to multiple members, we will refer to them in plural as *functions*,

although they are merely the function u evaluated as given parameter values $\{\boldsymbol{\alpha}_n\}$. We will also suppress the dependence of u on its domain, for simplicity of notation.

If there is a suitable basis $\mathcal{V}$ of $\mathcal{U}$ with small dimension M,

$$\mathcal{V} = \{v_1, v_2, ..., v_M\},$$

then a natural choice for approximating the solution u at a new parameter value $\boldsymbol{\alpha}$, is to construct $\tilde{u}$ that is a linear combination of the basis functions,

$$\tilde{u}(\boldsymbol{\alpha}) = \sum_{j=1}^{M} c_j(\boldsymbol{\alpha}) v_j. \tag{2.1}$$

There is a wealth of choices for the coefficients $c_j(\boldsymbol{\alpha})$, but they are typically chosen to minimize the error in some sense, for example $\sum_n \|\tilde{u}(\boldsymbol{\alpha}_n) - u_n\|_2^2$. When the coefficients are chosen in a way that this error vanishes (that is, $\tilde{u}(\boldsymbol{\alpha}_n) = u_n$) we call the approximation $\tilde{u}$ an interpolant.

Although linear approximation (or interpolation) is a very powerful tool, there are examples where linear approximation with respect to the parameters fail to be optimal, due to the fact that there exists no low-dimensional linear subspace $\mathcal{V}$, even though $\mathcal{U}$ may be low-dimensional in some other sense. An example of particular interest is when $u(\boldsymbol{\alpha})$ is the solution to a hyperbolic PDE. To demonstrate this difficulty, suppose the parameter is the time variable, $\boldsymbol{\alpha} = t$, and $u(t)$ is the solution to a 1-dimensional transport equation

$$\begin{cases} u_t + u_x = 0 & \text{in } (0,1), \\ u(x,0) = \phi(x - 3w), \\ u(0,t) = u(1,t), \end{cases} \tag{2.2}$$

where $w = 0.05$, and $\phi(x)$ is a hat function centered at 0 of width $2w$,

$$\phi(x; w) = \begin{cases} \frac{1}{w}(x + w) & \text{if } -w \le x \le 0, \\ -\frac{1}{w}(x - w) & \text{if } 0 \le x \le w, \\ 0 & \text{otherwise.} \end{cases} \tag{2.3}$$

Suppose that we are given $u(t)$ at various times $t_1 < t_2 < \cdots < t_M$ as shown in Figure 1. These functions $u(t_n)$ are all orthogonal to each other since $\operatorname{supp} u(t_n) \cap \operatorname{supp} u(t_m) = \emptyset$ for $n \neq m$, hence no low-dimensional basis $\mathcal{V}$ can be found for $\mathcal{U} = \{u(t_n)\}$. Nonetheless, the functions are merely translates of each other.

Naturally, our goal is to construct an interpolant $\tilde{u}(t)$ that satisfies $\tilde{u}(t_j) = u(t_j)$ that exploits this translation symmetry without having to compute additional solutions (that is, adding to $\mathcal{U}$) or adaptively refining the linear basis (adding to $\mathcal{V}$). We propose to construct an interpolant using *displacement interpolation* [26], by solving a simple optimal transport problem between the functions $\{u(t_n)\}$ then find the low-rank structure in the computed transport maps. To keep the operations as simple as possible, we make use of a simple optimal transport solution, called *monotone rearrangement* [25, 44]. The resulting solution is straightforward to compute, making it a potentially useful tool in a wide variety of contexts.

2.1. Monotone rearrangement. Suppose we wish to interpolate between two functions $u_1, u_2 > 0$ in $\mathcal{L} := L^2(\Omega) \cap L^\infty(\Omega)$ that satisfies

$$\int_\Omega u_1 \, dx = \int_\Omega u_2 \, dx = 1. \tag{2.4}$$

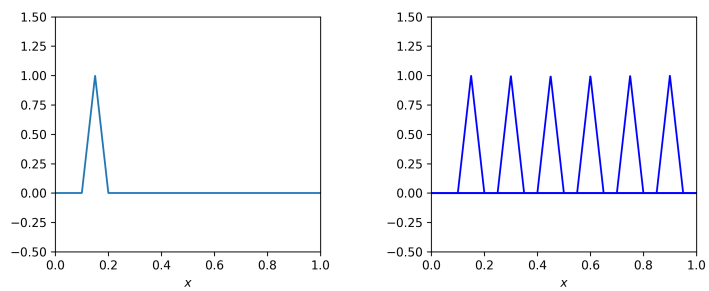

Fig. 1: The initial condition in (2.2), the hat function $\phi(x - 3w)$ with $w = 0.05$ (left). The solution of the advection equation (2.2) at different times $t_n = 3(n-1)w$ overlayed on top of each other, for $n = 1, 2, ..., 6$ (right).

In our setting, the two functions can be considered to be the parametrized function $u(\alpha)$ evaluated at two parameter values α_1 and α_2, that is, $u_1 = u(\alpha_1)$ and $u_2 = u(\alpha_2)$. In the optimal transport literature these two densities are referred to as probability distribution functions (PDFs), and we will follow this convention as long as the functions we are referring to are non-negative.

We define the optimal transport problem as:

$$\begin{aligned} \text{find } M \text{ that minimizes } & \int_\Omega |x - M(x)| u_1(x)\, dx, \\ \text{subject to } & u_1(M(x)) = u_2(x). \end{aligned} \tag{2.5}$$

This is a version of the mass transfer problem posed by Monge [22, 44], and the minimizing functional is called the Wasserstein metric [14]. The problem is well-known to be degenerate even in the simple 1-dimensional setting, as illustrated by the book-shifting example [17]. However, there is a particularly simple explicit formulation of the solution when $\Omega = \mathbb{R}$: we seek a non-decreasing function $U(x)$ such that

$$\int_{-\infty}^{x} u_1\, dx = \int_{-\infty}^{U(x)} u_2\, dx. \tag{2.6}$$

This solution is called monotone rearrangement, as it rearranges the mass in a monotone manner. Physically, this implies that particle trajectories do not cross, when they are transported across the domain by the transport map. Without loss of generality, we will first consider the case of approximating between two such 1-dimensional functions u_1 and u_2 that are positive in the domain $\mathbb{R}$. The restrictions on the dimension, the number of functions, and the strict positivity, will all be removed as we progress.

Upon differentiating (2.6), we obtain the ordinary differential equation

$$U'(x) = u_1(x) / u_2(U(x)), \tag{2.7}$$

valid when $u_1, u_2 > 0$ with regularity conditions, for example if u_1, u_2 are smooth.

As an alternative to solving the differential equation, we may compare the cumulative distribution functions (CDFs) of u_1 and u_2:

$$U_1(x) := \int_{-\infty}^{x} u_1(y)\, dy \quad \text{and} \quad U_2(x) := \int_{-\infty}^{x} u_2(y)\, dy. \tag{2.8}$$

Since u_1, u_2 are both positive U_1, U_2 are both strictly monotone increasing. Moreover, the CDFs are continuous hence the inverses of U_1 and U_2 exist. The CDF $\widetilde{U}_\lambda$ of the displacement interpolant (for given weight λ) is defined by letting its inverse equal the linear combination of U_1^{-1} and U_2^{-1}[12],

$$\widetilde{U}_\lambda^{-1}(y) := (1-\lambda)U_1^{-1}(y) + \lambda U_2^{-1}(y) \quad \text{where } 0 \le \lambda \le 1. \tag{2.9}$$

Then, letting $\lambda(\alpha)$ be the barycentric coordinate[1]of α with respect to the nodes $\{\alpha_1, \alpha_2\}$, the displacement interpolant is obtained by taking the derivative of its CDF,

$$\tilde{u}_\alpha := \mathcal{I}(\alpha; u_1, u_2) := \frac{d}{dx}\widetilde{U}_{\lambda(\alpha)}. \tag{2.10}$$

It is easy to see that $\tilde{u}_\alpha$ is indeed an interpolant; when $\alpha = \alpha_1$ ($\alpha = \alpha_2$) one recovers $\tilde{u}_\alpha = u_1$ ($\tilde{u}_\alpha = u_2$, respectively). We will also denote this interpolation by $\mathcal{I}(\alpha; u_1, u_2)$, as indicated above.

Nonetheless, this interpolant cannot be directly used for the 1D transport equation example above (2.2) because the solution u vanishes in some portions of the domain. Therefore, we next generalize the definition for the interpolant $\tilde{u}_\alpha$ (2.10), so that u_1, u_2 are allowed to be zero in some parts of the domain.

2.2. Two functions with non-negative values. In this section, we remove the requirement that u_1, u_2 both have to be strictly positive, and define the interpolation procedure for two functions with non-negative values. The intervals where these functions vanish appear as intervals in which the respective CDFs is constant. Now the CDFs are no longer invertible, but their graphs certainly can be reflected across the line $\{(x, y) : x = y\}$ and these intervals can be conveniently represented as Heaviside jump functions.

Suppose u_1, u_2 are allowed to vanish, that is, $u_1, u_2 \ge 0$. This implies that the CDFs U_1, U_2 may have intervals in which they are constant. We will restrict our discussion to functions u_1, u_2 for which there are only finitely many such intervals. Now, let us define a set of values for which $U_n(x)$ is constant,

$$\mathcal{Y}_n := \{y : U_n^{-1}(y) \text{ is not a singleton}\}, \quad \text{for } n = 1, 2, \tag{2.11}$$

then enumerate the members of the set $\mathcal{Y}_n$ in increasing order,

$$y_1^n < y_2^n < \cdots < y_k^n < \cdots < y_K^n.$$

We define the end-points of the intervals as follows,

$$a_k^n := \min\{U_n^{-1}(y_k^n)\} \quad \text{and} \quad b_k^n := \max\{U_n^{-1}(y_k^n)\},$$

and let $\ell_k^n = b_k^n - a_k^n$ denote the length of these intervals.

On the other hand, when $y \notin \mathcal{Y}_n$, the inverse $U_n^{-1}(y)$ is well-defined. Let us define W_n as the left limit of U_n^{-1} where it exists,

$$W_n(y) := \lim_{z \to y^+} U_n^{-1}(z).$$

We define $U_n^\dagger$ to be a *pseudo-inverse* of U_n in which the intervals where U_n is constant are represented using the Heaviside jump function H,

$$U_n^\dagger(y) := W_n(y) + \sum_{k=1}^{K} \ell_k^n \, H(y - y_k^n). \tag{2.12}$$

[1]Here, if $\alpha_1 < \alpha_2$ then $\lambda(\alpha) = (\alpha - \alpha_1)/(\alpha_2 - \alpha_1)$ for $\alpha_1 \le \alpha \le \alpha_2$.

Note that the pseudo-inverse encodes all the necessary information to recover U_n, so we can extend the interpolation previously defined in (2.9) for nonnegative profiles. The CDF $\widetilde{U}_\lambda$ of the displacement interpolant (for given weight λ) is naturally given in terms of its pseudo-inverse,

$$\widetilde{U}_\lambda^\dagger := (1-\lambda)U_1^\dagger(y) + \lambda U_2^\dagger(y) \quad \text{where } 0 \le \lambda \le 1. \tag{2.13}$$

Although $\widetilde{U}_\lambda^\dagger$ may involve Heaviside functions, one can uniquely determine $\widetilde{U}_\lambda$ from its pseudo-inverse defined here. Letting $\lambda(\alpha)$ denote the barycentric coordinate of α with respect to the nodes $\{\alpha_1, \alpha_2\}$, the interpolant is given by the derivative of the CDF,

$$\tilde{u}_\alpha := \mathcal{I}(\alpha; u_1, u_2) := \frac{d}{dx}\widetilde{U}_{\lambda(\alpha)}. \tag{2.14}$$

This removes the restriction that the two functions have to be strictly positive.

2.3. Two functions of arbitrary total mass. Suppose the two functions $u_1, u_2 \ge 0$ do not integrate to one. We can incorporate this additional generalization into our definition by simply scaling (2.14) by a multiplicative constant. We simply let

$$M_n := \int_{-\infty}^{\infty} u_n \, dx, \quad \text{for } n = 1, 2, \tag{2.15}$$

to normalize U_1, U_2, so that the linear combination (2.13) now becomes

$$\widetilde{U}_\lambda^\dagger(y) := (1-\lambda)U_1^\dagger(M_1 y) + \lambda U_2^\dagger(M_2 y) \quad \text{where } 0 \le \lambda \le 1. \tag{2.16}$$

Letting $\lambda(\alpha)$ denote the barycentric coordinate, we scale the interpolant linearly in the final step,

$$\tilde{u}_\alpha := \mathcal{I}(\alpha; u_1, u_2) := [(1-\lambda(\alpha))M_1 + \lambda(\alpha)M_2] \, \frac{d}{dx}\widetilde{U}_{\lambda(\alpha)}, \tag{2.17}$$

This guarantees that although the total integral of u_1 and u_2 are not the same, that of $\tilde{u}_\alpha$ will interpolate between the two values linearly, that is,

$$\int_{-\infty}^{\infty} \tilde{u}_\alpha \, dx = (1-\lambda(\alpha)) \int_{-\infty}^{\infty} u_1 \, dx + \lambda(\alpha) \int_{-\infty}^{\infty} u_2 \, dx.$$

2.4. Two functions with values of arbitrary sign. Now we remove the restriction that the two functions u_1 and u_2 have to be non-negative. We will separate the positive and negative parts and treat them separately. This marks a point of departure from the optimal transport problem (2.5), and our extension will not be a genuine extension of the optimal transport solution in many aspects. However, the extension here are intuitive and more suitable in our context of dimensionality reduction of responses with large convective effects. This straightforward strategy was also considered for defining the Wasserstein metric between such functions in [7, 49], but neither applies when any of the parts vanish, the case considered in (2.22) below. While this case may be negligible in other contexts, in hyperbolic problems wave profiles often reflect and propagate with negated sign, so it would be meaningful to construct a well-defined interpolation even for that case. In [49], it was also suggested

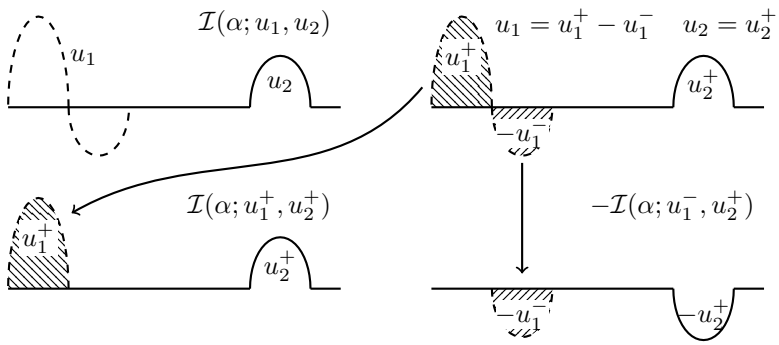

Fig. 2: Illustration for displacement interpolation of two functions u_1, u_2 of arbitrary sign when $u_2^- = 0$ (2.22), defined in terms of two interpolations of the non-negative cases (2.19). One treats the positive and negative parts (top row) by applying the interpolation for non-negative functions separately to both pairs (bottom row).

that a fixed constant c be added to $\{u_n\}$ to achieve positivity, but this addition of low-frequency content can cause the low-rank structures to be lost; see the concluding remarks of subsection 2.5.

Let us denote the postive and negative parts of u_1, u_2 as follows,

$$u_n^+ := \max\{u_n, 0\}, \quad u_n^- := \min\{u_n, 0\}, \quad \text{for } n = 1, 2. \tag{2.18}$$

If all of $u_1^+, u_1^-, u_2^+, u_2^-$ are nontrivial, we interpolate as above for u_n^+ and u_n^- separately as in (2.17) to obtain $\tilde{u}_\alpha^+$ and $\tilde{u}_\alpha^-$,

$$\tilde{u}_\alpha^+ := \mathcal{I}(\alpha; u_1^+, u_2^+) \quad \text{and} \quad \tilde{u}_\alpha^- := \mathcal{I}(\alpha; u_1^-, u_2^-), \tag{2.19}$$

and then take their difference to be the interpolant,

$$\tilde{u}_\alpha := \mathcal{I}(\alpha; u_1, u_2) := \tilde{u}_\alpha^+ - \tilde{u}_\alpha^-. \tag{2.20}$$

If any of $u_1^+, u_1^-, u_2^+, u_2^-$ vanishes, one uses the part of opposite sign to interpolate. As an example, suppose $u_2^- = 0$ but all the other parts are nonzero, we compute $\tilde{u}_\alpha^-$ as the interpolant between u_1^- and $-u_2^+$,

$$\tilde{u}_\alpha^+ := \mathcal{I}(\alpha; u_1^+, u_2^+) \quad \text{and} \quad \tilde{u}_\alpha^- := \mathcal{I}(\alpha; u_1^-, u_2^+), \tag{2.21}$$

but we combine them so that the integral of $\tilde{u}_\alpha$ is a linear interpolant,

$$\tilde{u}_\alpha := \mathcal{I}(\alpha; u_1, u_2) := \tilde{u}_\alpha^+ - \beta \tilde{u}_\alpha^-. \tag{2.22}$$

The coefficient β is determined by imposing that the integral of the interpolant should be a linear interpolant between the integral of u_1 and u_2 (that is, M_1 and M_2, respectively) as was done in (2.17),

$$\int_{-\infty}^{\infty} \tilde{u}_\alpha \, dx = \int_{-\infty}^{\infty} (\tilde{u}_\alpha^+ - \beta \tilde{u}_\alpha^-) \, dx = (1 - \lambda(\alpha)) M_1 + \lambda(\alpha) M_2. \tag{2.23}$$

Then one may easily compute β,

$$\beta = \frac{(1 - \lambda(\alpha)) M_1^- + \lambda(\alpha) M_2^-}{(1 - \lambda(\alpha)) M_1^- + \lambda(\alpha) M_2^+} \quad \text{where} \quad M_n^\pm := \int_{-\infty}^{\infty} u_n^\pm \, dx \quad \text{for } n = 1, 2. \tag{2.24}$$

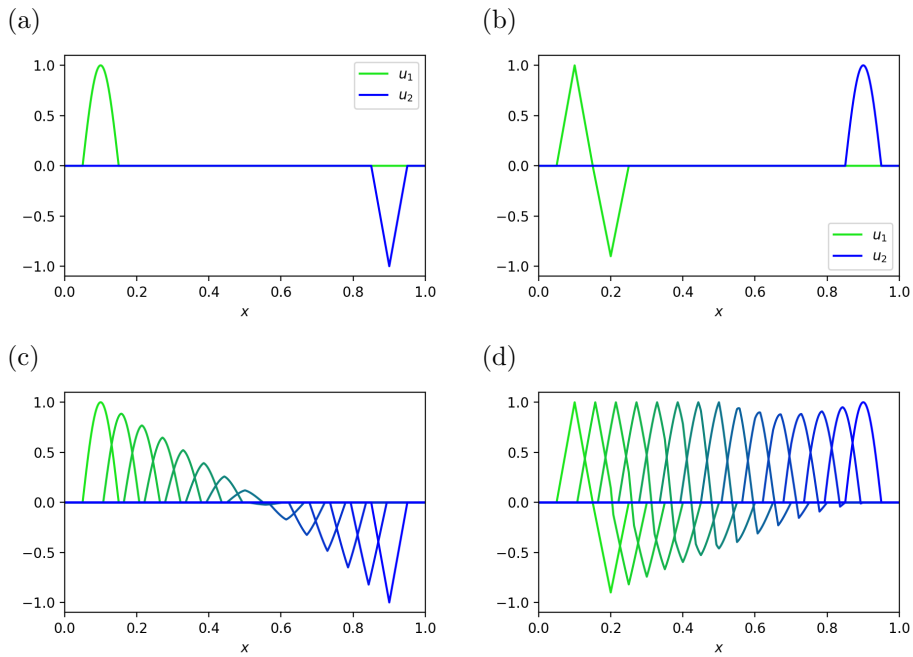

Fig. 3: Two functions u_1 and u_2 and their displacement interpolant defined by the interpolation procedure (2.22). The case when u_1^- and u_2^+ vanish (a,c), and the case only u_2^- vanishes (b,d).

Since $M_2^- = 0$ in this case, we have that

$$\beta = \frac{(1-\lambda(\alpha))M_1^-}{(1-\lambda(\alpha))M_1^- + \lambda(\alpha)M_2^+}. \tag{2.25}$$

Analogous definitions follow for other cases (when more of $u_n^\pm$ vanish.) Two representative examples are shown in Figure 3.

The extension suggested here appears natural for our applications, but it is by no means the only possible one. We also note that unlike the monotone rearrangement, the resulting interpolant defined here for arbitrary signs will not preserve the monotonicity in general. However, since we are simply interested in finding a low-dimensional structure in the transport maps thusly defined, the lack of monotonicity is not necessarily a serious concern.

On the other hand, it may be advantageous to adapt the interpolation procedure above by decomposing the derivatives of u_1 and u_2 into individual *pieces* with connected supports and apply the interpolation above between individual pairs, in relation to scalar conservation laws [5]. This interpolation procedure was called *displacement interpolation by pieces* and used in the construction of ROMs in [38]. This map will preserve monotonicity if the given functions satisfy the *signature condition* defined therein. We will show in subsection 2.7 that these extensions are merely special cases of a more general formulation.

2.5. More than two functions. Consider the case when we are given multiple functions, corresponding to the parametrized function evaluated at multiple parameter

values,

$$\mathcal{U} = \{u(\boldsymbol{\alpha}_1), u(\boldsymbol{\alpha}_2), ..., u(\boldsymbol{\alpha}_n)\}.$$

For simplicity of exposition, let us assume that all functions in $\mathcal{U}$ are non-negative. We wish to interpolate these functions with respect to the parameters $\boldsymbol{\alpha}$. Let us compute $U_n^\dagger$ for each $u_n = u(\boldsymbol{\alpha}_n)$ by the formula (2.12), and denote the set of these CDFs by $\mathcal{U}^\dagger = \{U_n^\dagger : n = 1, ..., N\}$. Then we can extend the interpolation procedure, by generalizing the definition of the CDF of the interpolant (2.13) in a piece-wise linear manner,

$$\widetilde{U}_{\boldsymbol{\alpha}}^\dagger := \sum_{n=1}^{N} \lambda_n(\boldsymbol{\alpha})\, U_n^\dagger. \tag{2.26}$$

There is a freedom in choosing $\lambda_n(\boldsymbol{\alpha})$ but we will choose it to be the barycentric coordinates for conceptual simplicity. For more general discussions on Wasserstein barycenters, see [2]. That is, $\{\boldsymbol{\alpha}_n\}$ will serve as nodes (or vertices) of a tessellation, and $\lambda_n(\boldsymbol{\alpha})$ will yield the barycentric coordinate with respect to the nodes of the polytope $\boldsymbol{\alpha}$ belongs to.

Further suppose that $\mathcal{U}^\dagger$ has a low-rank representation with the corresponding low-dimensional basis $\mathcal{V}^\dagger = \{V_n^\dagger : n = 1, ...M\}$. Then, the interpolant can be computed in a similar manner as was done for the linear approximation (2.1),

$$\widetilde{U}_{\mathrm{LR},\boldsymbol{\alpha}}^\dagger := \sum_{n=1}^{N} \nu_n(\boldsymbol{\alpha})\, V_n^\dagger. \tag{2.27}$$

for coefficients ν_n that depend on $\boldsymbol{\alpha}$. Therefore we obtain a low-dimensional representation $\widetilde{U}_{\mathrm{LR},\boldsymbol{\alpha}}^\dagger$ in terms of the optimal transport map. Then $\tilde{u}_{\boldsymbol{\alpha}}$ is given by the analogue of (2.17),

$$\tilde{u}_{\boldsymbol{\alpha}} := \mathcal{I}(\boldsymbol{\alpha}; u_1, \cdots, u_N) := \left[\sum_{n=1}^{N} \nu_n(\boldsymbol{\alpha}) M_n\right] \frac{d}{dx} \tilde{U}_{\mathrm{LR},\boldsymbol{\alpha}} \tag{2.28}$$

Straightforward adjustments to (2.26) and (2.27) can be made for the case when the functions take on arbitrary signs. The basis functions $\{V_n\}$ in (2.27) were named *advection modes* in [21], although the modes here can be computed explicitly without any optimization. In order to demonstrate that the interpolant $\tilde{u}_{\boldsymbol{\alpha}}$ is useful, let us revisit the 1D transport example (2.2). Suppose we were given the set of solutions to the transport equation,

$$\mathcal{U} = \{u(t_n) : n = 1, ..., 6\} \quad \text{where } t_n = 3w(n-1), \quad (w = 0.05),$$

as was shown in Figure 1. If one computes the CDFs $\{U_n\}$ for each $u_n = u(t_n)$, as shown in Figure 4, one discovers that their pseudo-inverses are

$$U_n^\dagger(y) = 3w(n-1)H(y) + U_1^\dagger(y). \tag{2.29}$$

This shows that translation is a low-dimensional operation when viewed in the form (2.27), representable by the addition of a Heavside function. That is, although direct application of low-rank approximations such as the singular value decomposition (SVD) will not succeed in finding a low-rank approximation directly with $\{u_n\}$, it can be successfully applied to the CDFs $\{U_n^\dagger\}$. See subsection 3.4 for a related example.

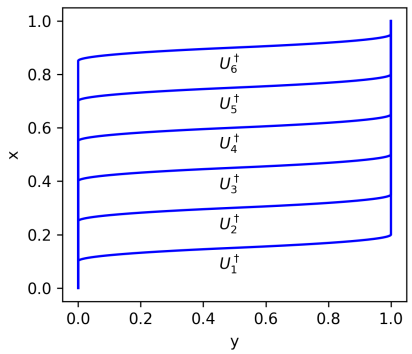

Fig. 4: Plot of $U_n^\dagger$ corresponding to the six hat functions to the right of Figure 1.

We remark that an addition of a constant value to $u(t_j)$ can affect this low-rank property for this problem. Just as linear operation such as the addition by a constant in the y variable result in rank-increasing operations (translation) in the x variable, linear operations in x can result in an increase of rank as functions in the y variable. This implies that some simple preprocessing of the functions may be necessary for this approach to be successful in general, e.g, the application of these methods to the derivative $\partial u_n/\partial x$ instead of u_n, as is done when applying displacement interpolation by pieces [38]. This was also observed in [7] where low-band modes were treated independently. This being said, the issue appears to be easy to circumvent and did not significantly affect the applicability of the interpolation method in our examples.

2.6. Multiple spatial dimensions. We have so far defined the displacement interpolation $\mathcal{I}$ (2.10, 2.17, 2.22) in a single spatial dimension. This definition can be naturally extended to multiple dimensions, and one approach is to consider the multi-dimensional Monge-Kantorovich optimal transport problem [4]. However, the multi-dimensional problem itself requires a solution of a nontrivial problem, e.g., the Monge-Ampère equation or related optimization problem which makes the resulting interpolant implicit and expensive to compute. To avoid such hurdles we instead propose a multi-dimensional extension which makes use of the intertwining property of the Radon transform [19, 29, 23, 35]. Note that this extension was also explored in the image processing literature [31, 6] as a method for avoiding the high computational cost of solving the multi-dimensional optimal transport problem.

Suppose u is a function of multiple spatial dimensions (e.g. $d = 2, 3$). The Radon transform of u is a function of $s \in \mathbb{R}$ and $\boldsymbol{\omega} \in S^{d-1}$, defined as the integral over the hyperplane oriented by s and $\boldsymbol{\omega}$,

$$\mathcal{R}\left[u\right](s, \boldsymbol{\omega}) := \int_{\mathbf{x}\cdot\boldsymbol{\omega}=s} u(\mathbf{x})\, dm(\mathbf{x}), \tag{2.30}$$

where $m(\mathbf{x})$ is the Euclidean measure over the hyperplane $\{\mathbf{x} \in \mathbb{R}^d : \mathbf{x}\cdot\boldsymbol{\omega} = s\}$.

The main property of this transform we will be interested in is the intertwining property [19, 29],

$$\mathcal{R}\left[\frac{\partial u}{\partial x_i}\right](s, \boldsymbol{\omega}) = \omega_i \left(\frac{\partial}{\partial s}\mathcal{R}\left[u\right]\right)(s, \boldsymbol{\omega}), \tag{2.31}$$

where ω_i is the i-th component of $\boldsymbol{\omega}$. For example, the multi-dimensional transport equation

$$u_t + \boldsymbol{\theta} \cdot \nabla u = 0 \quad \text{where } \boldsymbol{\theta} \in S^{d-1},$$

for u is transformed into a collection of 1D transport equations for $\mathcal{R}[u]$, where the transport speed for each 1D problem now depends on $\boldsymbol{\omega}$,

$$\mathcal{R}\left[u\right]_t + \left(\boldsymbol{\theta} \cdot \boldsymbol{\omega}\right) \mathcal{R}\left[u\right]_s = 0. \tag{2.32}$$

This property is useful not only for the transport equation, but other hyperbolic PDEs such as the acoustics equations. We refer to [35] for further details.

A natural extension of the displacement interpolation procedure $\mathcal{I}$ in 1D defined in the previous sections is to perform the interpolation for each fixed $\boldsymbol{\omega}$ in the transformed variable s. That is, given two multi-dimensional PDFs $u_1, u_2 \geq 0$, we define the displacement interpolant in terms of its Radon transform,

$$\mathcal{R}\left[\tilde{u}_\alpha\right](\cdot, \boldsymbol{\omega}) := \mathcal{I}\left(\alpha; \mathcal{R}\left[u_1\right](\cdot, \boldsymbol{\omega}), \mathcal{R}\left[u_2\right](\cdot, \boldsymbol{\omega})\right) \tag{2.33}$$

We will also denote the interpolation that appears on the RHS of (2.33) by

$$\mathcal{I}_\otimes\left(\alpha; \mathcal{R}\left[u_1\right], \mathcal{R}\left[u_2\right]\right), \tag{2.34}$$

where $\mathcal{I}_\otimes$ acts on the s-variable of the transform individually. We now invert the transform to obtain $\tilde{u}_\alpha$,

$$\tilde{u}_\alpha := \mathcal{I}_d(\alpha; u_1, u_2) := \mathcal{R}^{-1}\left[\mathcal{R}[\tilde{u}_\alpha]\right]. \tag{2.35}$$

The inversion $\mathcal{R}^{-1}$ is ill-posed, but unlike in the more common tomography setting one can reduce the inversion error simply by over-sampling the forward data. For a more detailed discussion, we refer the reader to [35, 36]. In section 3, we will see that this explicit construction yields reasonable numerical results. We will call this interpolation operator the *generalized Lax-Philips operator*, as it generalizes the translation representation of the one-parameter family of solutions to the wave equation by Lax-Philips [23] to representations using monotone rearrangement.

To the best of our knowledge, it has not yet been rigorously investigated whether this particular construction $\tilde{u}_\alpha$ is a solution to a multi-dimensional optimal transport problem, perhaps a variant of (2.5). We will not pursue such an undertaking here, and leave the task to a future work.

2.7. Composition with general transforms. The application of the Radon transform in subsection 2.6 suggests that the interpolant can achieve a rich set of behavior when applied together with the right transform. We formally define such a displacement interpolation procedure in this section. Let us denote an invertible transform by $\mathcal{T}$. We define $\mathcal{I}_\mathcal{T} : \mathcal{L} \times \mathcal{L} \to \mathcal{L}$ by a conjugation of $\mathcal{I}_\otimes$,

$$\mathcal{I}_\mathcal{T} := \mathcal{T}^{-1} \mathcal{I}_\otimes \mathcal{T}. \tag{2.36}$$

Note that the dependence on the interpolation parameter α is omitted here. If the operands are 1D functions, let $\mathcal{I}_\otimes = \mathcal{I}$.

As an elementary example, the operation of separating the positive and negative parts as in subsection 2.4 can be formulated differently. For the case when neither the positive nor the negative parts vanish, the transform $\mathcal{T}$ may be given by

$$\mathcal{T}[u] = [\max\{u, 0\}, \max\{-u, 0\}] \quad \text{and} \quad \mathcal{T}^{-1}[u^+, u^-] = u^+ - u^-. \tag{2.37}$$

Similar definitions could be made for the other cases discussed in subsection 2.4. Displacement interpolation by pieces in [38] could also be expressed in this form.

We will remark on how (2.36) serves to unify the various interpolants based on the monotone rearrangement in 1D that appear here and elsewhere under one framework. The generalized Lax-Philips operator (2.35) is a special case of the above when one lets $\mathcal{T} = \mathcal{R}$. We also note that the operator $\mathcal{I}_\otimes$ could have been applied to the $\boldsymbol{\omega}$-variable as an alternative. One obvious choice for $\mathcal{T}$ could be the derivative operator; see subsection 3.5. In image processing, choosing $\mathcal{T}$ to be the Fourier transform or wavelet transform was shown to be useful for color or texture mixing [6, 33]. The treatment of low-frequency components in [7] can also be related to by (2.36).

In our numerical example in subsection 3.8, we will show that $\mathcal{T} = \mathcal{R} \otimes \mathcal{P}\mathcal{F}$ for some permutation $\mathcal{P}$ can capture the low-rank structure of oscillatory functions.

3. Numerical implementation and examples. In this section, we discuss some issues related to implementation and provide some numerical examples that illustrate the behavior of the displacement interpolant introduced in the previous sections.

3.1. Implementation. In the discretized setting, the function u_n in the previous sections will be represented as a vector $\mathbf{u}_n$ in $\mathbb{R}^D$. We will choose a piece-wise constant representation of the function u_n. The reason for this is simplicity, as the exact cumulative distribution function U_n defined in (2.8) will then be piece-wise linear. This is convenient since we plan to perform linear operations on $U_n^\dagger$, e.g., to interpolate between two profiles in (2.13), or to compute low-rank linear bases for multiple profiles in (2.27). A higher-order representation of u_n will cause the exact representation of $U_n^\dagger$ to involve fractional powers of y (such as the square root) which is cumbersome to work with, especially when the grid-points are not uniform in terms of the variable U_n.

To be more precise, let us suppose that $\mathbf{u}_n$ represents u_n by its integral over cells of uniform width h, i.e., $x_{j+1/2} = jh$,

$$(\mathbf{u}_n)_j = \frac{1}{h}\int_{x_{j-1/2}}^{x_{j+1/2}} u_n \, dx.$$

Now, let us denote by $\mathbf{U}_n$ the cumulative distribution of $\mathbf{u}_n$ when viewed in its piece-wise constant representation. The result will be a piece-wise linear function and will serve as a discretization of U_n, a linear interpolant through the points $\sum_{k=1}^{j}(\mathbf{u}_n)_k$ on the same uniform grid $\{x_j\}$.

To compute the pseudo-inverse $U_n^\dagger$ one simply exchanges the two entries of the interpolating points. That is

$$(x_{j+1/2}, (\mathbf{U}_n)_j) \quad \to \quad ((\mathbf{U}_n)_j, x_{j+1/2}).$$

We will define $\mathbf{U}_n^\dagger$ as the linear interpolant of these points. When represented as a 2D array, for example, we can write

$$(\mathbf{U}_n^\dagger)_{j,1} = (\mathbf{U}_n)_j \quad \text{and} \quad (\mathbf{U}_n^\dagger)_{j,2} = x_{j+1/2}.$$

However, although $(\mathbf{U}_n)_j$ is non-increasing, it does not form a uniform grid in general, and there will be redundant entries if $\mathbf{u}_n$ vanishes. So some care must be taken when computing linear operations such as (2.13) on $\mathbf{U}_n^\dagger$. One simple solution would be to merge the grid $(\mathbf{U}_n)_j$ whenever two pseudo-inverses are added, and in the worst

case the size of the array will grow linearly with the number of operations. We will make this choice for the implementation presented here as the interpolation procedure will be exact and free from approximation errors, but one may opt for a fixed grid interpolation away from the points in $\mathcal{Y}$ where U_n is constant (2.11) for efficiency. The implementation we have used is available in a public online repository [37].

To compute the Radon transform (2.30), we will make use of a fast approximate algorithm called the Discrete Radon Transform (DRT) [8, 32, 35]. To control the inversion error, the inverse is computed using the conjugate gradient algorithm [18] on the prolongated transform. While the computational cost for the inversion could be high, it is still conjectured to be $\mathcal{O}(D^{5/2}\log D)$ when the 2-dimensional functions u_n are each represented on the grid of size $D \times D$ (so that $\mathbf{u}_n$ is in $\mathbb{R}^{D\times D}$). Further improvements in the inversion algorithms may reduce this computational burden, but this topic is also left as future work.

3.2. 1D interpolation with 2D parameters. In this section, we will illustrate the behavior of the displacement interpolant defined above by computing the interpolant between three different functions u_1, u_2, u_3 functions, using the barycentric formula. These three functions are shown in Figure 5. The function u_1 is a sum of two hat functions ϕ (2.3) with different heights and positions, and the function u_2 is a sharp hump which can be represented by a sum of two Heaviside jump functions. The function u_3 is a superposition of two functions in the form of u_2. These functions are neither translates of each other nor do they have identical number of connected supports. In other words, if one recalls the definition of $\mathcal{Y}_n$ (2.11), we have that $|\mathcal{Y}_1| = |\mathcal{Y}_3| = 3$ whereas $|\mathcal{Y}_2| = 2$. Also, total mass is distributed differently between the two superposed profiles in u_1 and u_3. These functions are shown in Figure 5. The corresponding CDFs are shown in Figure 6.

The displacement interpolant we will compute will be of the form (2.26), where for the coefficients c we will use the barycentric coordinates λ. We will suppose that

$$u_1 = u(\boldsymbol{\alpha}_1), \quad u_2 = u(\boldsymbol{\alpha}_2), \quad u_3 = u(\boldsymbol{\alpha}_3),$$

where the parameter values are given by

$$\boldsymbol{\alpha}_1 = (0,0), \quad \boldsymbol{\alpha}_2 = (1,0), \quad \boldsymbol{\alpha}_3 = (0,1).$$

Then the displacement interpolant is written as

$$\tilde{u}_{\boldsymbol{\alpha}} = \mathcal{I}_{\lambda(\boldsymbol{\alpha})}(\boldsymbol{\alpha}; u_1, u_2, u_3), \tag{3.1}$$

whose pseudo-inverse of the CDF $\widetilde{U}^\dagger$ is computed by

$$\begin{aligned} \widetilde{U}^\dagger_{\boldsymbol{\alpha}} &= \lambda_1(\boldsymbol{\alpha})U_1^\dagger + \lambda_2(\boldsymbol{\alpha})U_2^\dagger + \lambda_3(\boldsymbol{\alpha})U_3^\dagger \\ &= (1-\alpha_1-\alpha_2)U_1^\dagger + \alpha_1 U_2^\dagger + \alpha_2 U_3^\dagger. \end{aligned} \tag{3.2}$$

We will evaluate $\tilde{u}_{\boldsymbol{\alpha}}$ at the nodes in the convex hull of $\{\boldsymbol{\alpha}_1, \boldsymbol{\alpha}_2, \boldsymbol{\alpha}_3\}$ shown as white circles in Figure 5 with respective enumeration. The nodes are,

$$\begin{aligned} &\tilde{\boldsymbol{\alpha}}_1 = (0.25, 0), && \tilde{\boldsymbol{\alpha}}_4 = (0.75, 0.25), && \tilde{\boldsymbol{\alpha}}_7 = (0, 0.75), && \tilde{\boldsymbol{\alpha}}_{10} = (0.25, 0.25), \\ &\tilde{\boldsymbol{\alpha}}_2 = (0.5, 0), && \tilde{\boldsymbol{\alpha}}_5 = (0.5, 0.5), && \tilde{\boldsymbol{\alpha}}_8 = (0, 0.5), && \tilde{\boldsymbol{\alpha}}_{11} = (0.5, 0.25), \\ &\tilde{\boldsymbol{\alpha}}_3 = (0.75, 0), && \tilde{\boldsymbol{\alpha}}_6 = (0.25, 0.75), && \tilde{\boldsymbol{\alpha}}_9 = (0, 0.25). && \tilde{\boldsymbol{\alpha}}_{12} = (0.25, 0.5). \end{aligned} \tag{3.3}$$

Figure 7 displays the displacement interpolant $\tilde{u}$ at the nodes $\tilde{\boldsymbol{\alpha}}_1, \tilde{\boldsymbol{\alpha}}_2, \tilde{\boldsymbol{\alpha}}_3$, and shows a gradual deformation of u_1 into u_2. One notices that the acute angle at the

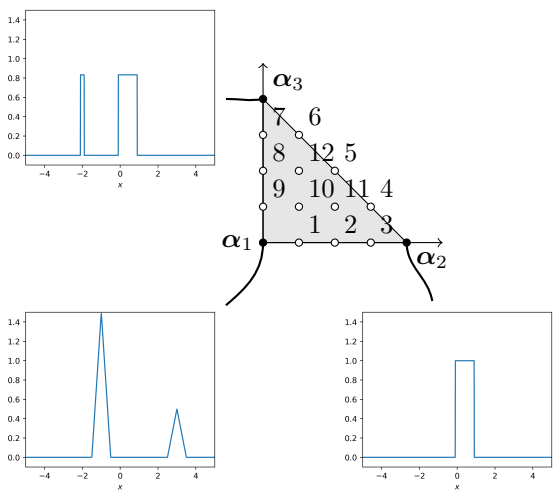

Fig. 5: The three functions $u_1 = u(\boldsymbol{\alpha}_1)$,$u_2 = u(\boldsymbol{\alpha}_2)$, $u_3 = u(\boldsymbol{\alpha}_3)$, corresponding to parameter values $\boldsymbol{\alpha}_1 = (0,0)$ $\boldsymbol{\alpha}_2 = (1,0)$, $\boldsymbol{\alpha}_3 = (0,1)$. The convex hull of $\{\boldsymbol{\alpha}_1, \boldsymbol{\alpha}_2, \boldsymbol{\alpha}_3\}$ is also displayed along with nodes where the inteprolants will be computed enumerated 1 to 12. The computed interpolants are shown in subsequent Figures 7 to 10.

tip of the two linear hat functions of u_1 gradually relax towards a horizontal line. The two peaks also are transported towards each other, about to merge into the profile of u_2. In Figure 8 we see $\tilde{u}_{\boldsymbol{\alpha}}$ evaluated at the nodes $\tilde{\boldsymbol{\alpha}}_4, \tilde{\boldsymbol{\alpha}}_5, \tilde{\boldsymbol{\alpha}}_6$. The one sharp hump in u_2 is split into two sharp humps and is scaled and transported to become u_3. The monotone rearrangement (2.6) ensures that the initial split takes place precisely at the ratio between the mass of two sharp humps in u_3. In Figure 9, $\tilde{u}_{\boldsymbol{\alpha}}$ is evaluated at $\tilde{\boldsymbol{\alpha}}_7, \tilde{\boldsymbol{\alpha}}_8, \tilde{\boldsymbol{\alpha}}_9$, the two sharp profiles in u_3 are deformed into u_1, and since the hump to the left does not contain enough mass to form the large hat function on the left in u_1, a bulk of mass is taken from the right hump. As parameter approaches that of $\boldsymbol{\alpha}_1$ the profiles sharpen and form a peak. The left two peaks will merge to form one hat function. In Figure 10 the displacement interpolant at $\tilde{\boldsymbol{\alpha}}_{10}, \tilde{\boldsymbol{\alpha}}_{11}, \tilde{\boldsymbol{\alpha}}_{12}$ are shown. These corresponds to interior points, and we observe interesting behavior of three hump functions of various shapes.

The behavior is predictable and natural, and the location of the profiles as well as their shapes are adjusted smoothly according to the paramters. This is in contrast to linear interpolation, where the basis functions are largely stationary.

3.3. Wavelets. It is straightforward to see the continuous wavelet basis [10] as a special case of a two-parameter version of (2.26) (or (3.2)), with $u_1(x)$ taken as a *wavelet function* $\psi(x)$. We perform the following displacement interpolation,

$$\zeta(x;\alpha_1,\alpha_2) := \mathcal{I}(\alpha_1,\alpha_2;u_1,u_2,u_3), \qquad \text{where} \begin{cases} u_1(x) = \psi(x), \\ u_2(x) = \psi(x/2)/\sqrt{2}, \\ u_3(x) = \psi(x-1). \end{cases} \tag{3.4}$$

The interpolants are shown in Figure 11. The continuous wavelet basis $\{\psi_{a,b}(x)\}$ is constructed by scaling and translating $\psi(x)$, which is related to the above interpolation

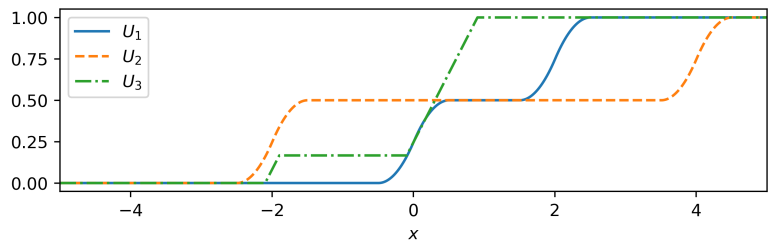

Fig. 6: The cumulative distribution functions (CDFs) of the functions u_1, u_2 and u_3, denoted by U_1, U_2 and U_3, respectively.

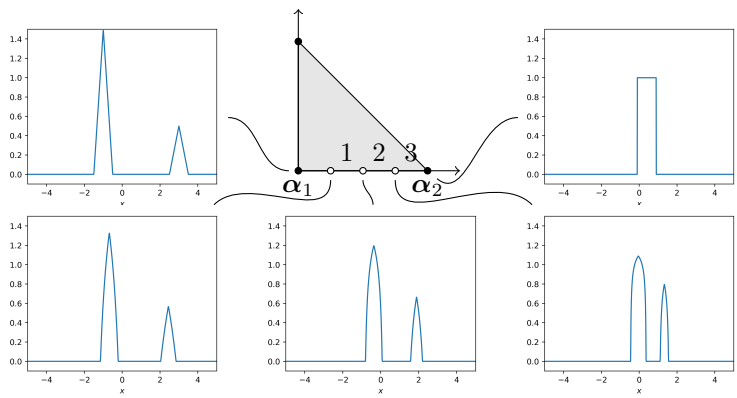

Fig. 7: The displacement interpolants $\tilde{u}_{\boldsymbol{\alpha}}$ for the values $\tilde{\boldsymbol{\alpha}}_1, \tilde{\boldsymbol{\alpha}}_2$, and $\tilde{\boldsymbol{\alpha}}_3$. The specific values are listed in (3.3).

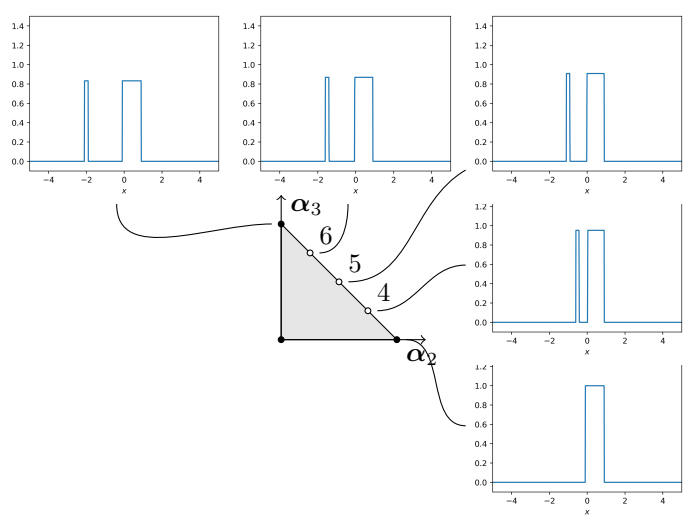

Fig. 8: The displacement interpolants $\tilde{u}_{\boldsymbol{\alpha}}$ for the values $\tilde{\boldsymbol{\alpha}}_4, \tilde{\boldsymbol{\alpha}}_5$, and $\tilde{\boldsymbol{\alpha}}_6$. The specific values are listed in (3.3).

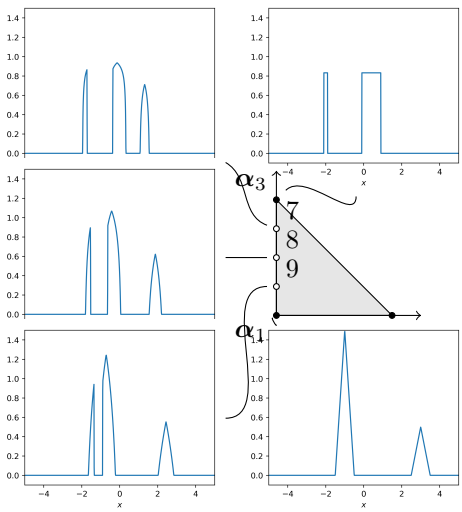

Fig. 9: The displacement interpolants $\tilde{u}_{\boldsymbol{\alpha}}$ for the values $\tilde{\boldsymbol{\alpha}}_7, \tilde{\boldsymbol{\alpha}}_8$, and $\tilde{\boldsymbol{\alpha}}_9$. The specific values are listed in (3.3).

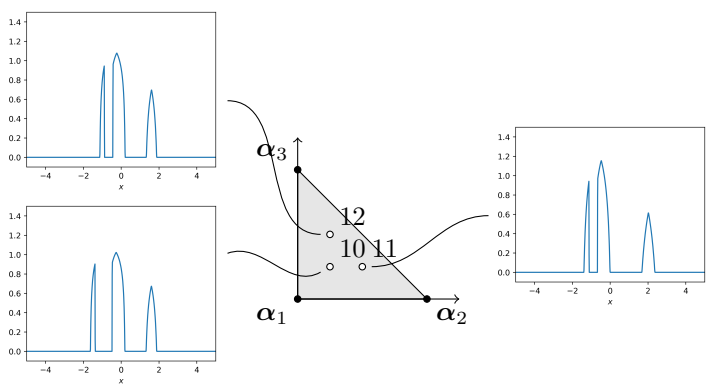

Fig. 10: The displacement interpolants $\tilde{u}_{\boldsymbol{\alpha}}$ for the values $\tilde{\boldsymbol{\alpha}}_{10}, \tilde{\boldsymbol{\alpha}}_{11}$, and $\tilde{\boldsymbol{\alpha}}_{12}$. The specific values are listed in (3.3).

$\mathcal{I}(\alpha_1, \alpha_2)$ with

$$\psi_{a,b}(x) = |a|^{-\frac{1}{2}} \psi\left(\frac{x-b}{a}\right) = C(a,b)\zeta\left(x;\, a, \frac{b}{a}\right). \tag{3.5}$$

Therefore the wavelet basis results from ζ in (3.4) up to a scalar multiple C.

In this sense, the displacement interpolation produces a generalization of the wavelet basis, beyond simple operations like dilation or translation. This observation can be expressed as an expansion in the characteristic variables, see [21, 38].

3.4. Multiple hat functions. Here we will revisit the example of multiple hat functions displayed in Figure 1. Recall the definition of hat functions $\phi(x; w)$ (2.3).

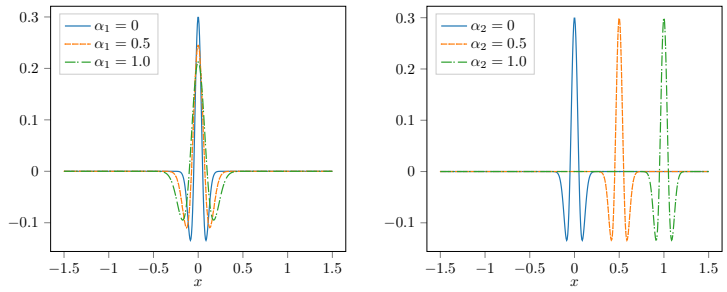

Fig. 11: Plot of the Mexican hat wavelet function $\psi(x)$ and its displacement interpolants $\zeta(x; \alpha_1, \alpha_2)$ defined in (3.4) for parameter weights $\alpha_1 = 0, 0.5, 1$ resulting in scaling (left), and $\alpha_2 = 0, 0.5, 1$ resulting in translation (right).

Let us define a collection of these hat functions with two parameters, the translate t and the width w,

$$\mathcal{U} = \{\phi(x - t, w) : 0.1 < t < 0.9, 0 < w < 0.1\}. \tag{3.6}$$

We will draw functions from $\mathcal{U}$ at random, by selecting random values of t and w with the uniform distribution over their allowed intervals to form $\mathcal{U}_n = \{u_n\}$. Then we compute the SVD of the snapshot matrix A whose $(n-1)$-th column is the difference of normalized pseudo-inverses $U_n^\dagger - U_1^\dagger$ (2.26),

$$A = \left[\cdots, \quad \frac{U_n^\dagger - U_1^\dagger}{\left\| U_n^\dagger - U_1^\dagger \right\|_2}, \quad \cdots \right]. \tag{3.7}$$

The matrix A is just a normalization of the gradient of $\widetilde{U}_{\boldsymbol{\alpha}}^\dagger$ with respect to α_j in (2.26). We see that there are two singular values that are the most significant as shown in Figure 12. The singular vectors corresponding to these singular values coincide roughly with translation and dilation, as also shown in the same figure. One may compare these singular vectors with the case when only translation is present, as displayed in Figure 4.

3.5. 1D acoustics equations. Consider the 1D acoustics equations for pressure p and velocity u,

$$\begin{bmatrix} p \\ u \end{bmatrix}_t + \begin{bmatrix} 0 & K_0 \\ 1/\rho_0 & 0 \end{bmatrix} \begin{bmatrix} p \\ u \end{bmatrix}_x = 0, \tag{3.8}$$

where K_0 is the bulk modulus and ρ_0 is the density. Let us suppose the initial condition for the pressure $p(x, 0)$ is given by the hat function (2.3) that is translated $\phi(x - 2w)$ with $w = 0.05$, and $u(x, 0) = 0$. Then the pressure at time t is given by

$$p(x, t) = \frac{1}{2}[\phi(x - 2h - ct; h) + \phi(x - 2h + ct; h)] \quad \text{where } c = \sqrt{K_0/\rho_0}. \tag{3.9}$$

For simplicity, let us assume that $K_0 = \rho_0 = 1$, so that $c = 1$. Suppose we are interested in the behavior of the pressure p with respect to the paramter $\alpha = t$, the time variable. We are given the solution at time $t_1 = 0$ and $t_2 = 3$, as shown in the

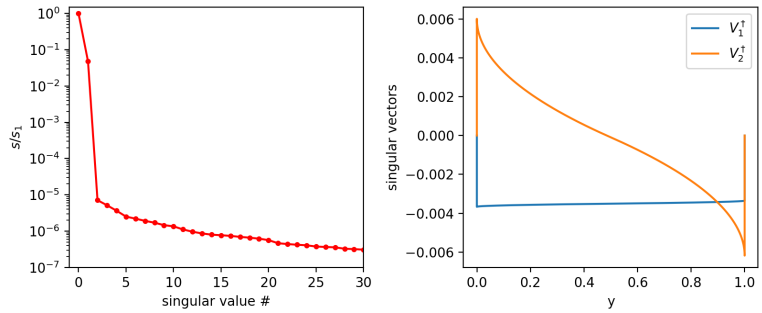

Fig. 12: Semi-log plot of scaled singular values s/s_1 of the snapshot matrix (3.7) (left) and the two leading singular vectors (right). $V_1^\dagger$ and $V_2^\dagger$ correspond roughly to translation and dilation; see Figure 4 for comparison.

.

top row of Figure 13, and we will use the displacement interpolant to approximate the solution times between t_1 or t_2.

Let us make an observation regarding the example in subsection 3.2. When the number of connected supports of the two given functions are different, the interpolation allocates the probability mass correspondingly and then divides the support. An example of this is shown in Figure 7. However, this behavior is different from that of the d'Alembert solution given in (3.9), where two copies of smaller amplitudes are produced then are transported in opposite directions. In what follows we will show that, for the given initial condition above, the wave-like behavior of the d'Alembert solution can be reproduced by applying the interpolation procedure to the derivatives of the given functions instead.

First, let us define $p_n(x) = p(x, t_n)$ for $n = 1, 2$ then compute

$$
\begin{aligned}
p_n^{d+d+} &:= \left[\frac{d}{dx}\left(\frac{dp_n}{dx}\right)^+\right]^+, \qquad & p_n^{d-d+} &:= \left[\frac{d}{dx}\left(\frac{dp_n}{dx}\right)^-\right]^+, \\
p_n^{d+d-} &:= \left[\frac{d}{dx}\left(\frac{dp_n}{dx}\right)^+\right]^-, \qquad & p_n^{d-d-} &:= \left[\frac{d}{dx}\left(\frac{dp_n}{dx}\right)^-\right]^-.
\end{aligned} \tag{3.10}
$$

In the continuous setting, these functions will be linear combinations of delta functions, but in a discretized setting these will be piece-wise constant functions whose support is contained in one grid cell.

Then we compute the interpolants

$$
\begin{aligned}
\tilde{p}_t^{d+d+} &:= \mathcal{I}(t; p_1^{d+d+}, p_2^{d+d+}), \quad & \tilde{p}_t^{d-d+} &:= \mathcal{I}(t; p_1^{d-d+}, p_2^{d-d+}), \\
\tilde{p}_t^{d+d-} &:= \mathcal{I}(t; p_1^{d+d-}, p_2^{d+d-}), \quad & \tilde{p}_t^{d-d-} &:= \mathcal{I}(t; p_1^{d-d-}, p_2^{d-d-}).
\end{aligned} \tag{3.11}
$$

To compute the interpolant we first obtain the corresponding CDFs (2.8) for $p_n^{d\pm d\pm}$ for $n = 1, 2$,

$$
P_n^{d\pm d\pm}(x) := \int_{-\infty}^{x} p_n^{d\pm d\pm}(y)\, dy, \tag{3.12}
$$

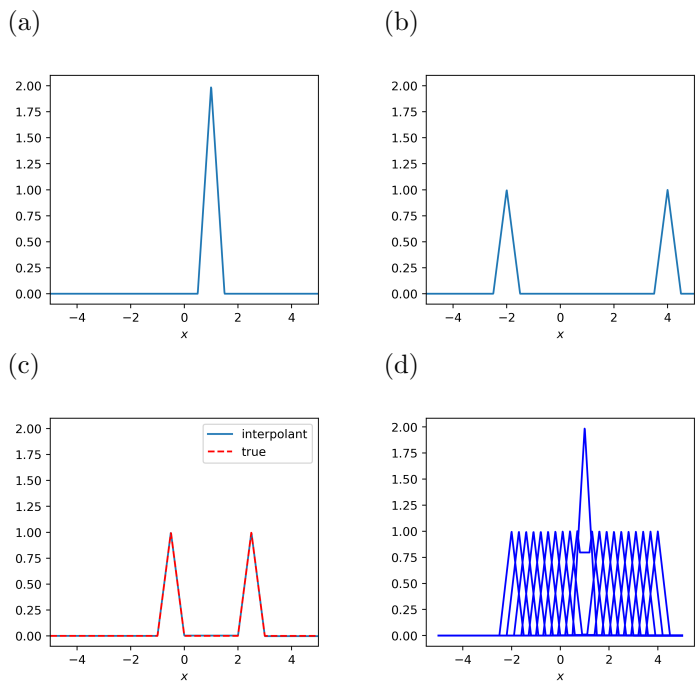

Fig. 13: (a) Solution for the pressure variable p to the 1D acoustics equations(3.8) at times $t_1 = 0$ and (b) $t_2 = 3$. (c) Displacement interpolant $\tilde{p}_t$ (3.11) to these two at $t = 1.5$ or $\lambda(t) = 0.5$, and (d) $\tilde{p}_t$ at times $t = 0.2n$ for $n = 0, 1, 2, ..., 10$.

.

which are plotted in Figure 14.

The interpolant is given by summing and integrating,

$$\tilde{p}_t := \int_{-\infty}^{x} \int_{-\infty}^{y} \left(\tilde{p}_t^{d+d+}(z) - \tilde{p}_t^{d+d-}(z) + \tilde{p}_t^{d-d+}(z) - \tilde{p}_t^{d-d-}(z) \right) \, dz \, dy. \tag{3.13}$$

The interpolant $\tilde{p}_t$ at $t = 1.5$ is shown in in Figure 13(c). It agrees exactly with the true pressure $p(x, 1.5)$, successfully translating the two hat functions with two opposite speeds. It is not difficult to verify that $\tilde{p}_t$ is equal to the exact solution for all values $0 < t < 3$. The plot of $\tilde{p}_t$ for 11 different values $t_n = 0.2n$ for $n = 0, 1, 2, ..., 10$ is shown in the lower right plot in Figure 13(d).

This demonstrates that for functions whose connected supports are being translated together with some speed, monotone rearrangement can be used to exploit the low-dimensional structure by utilizing the linear subspace formed by the pseudo-inverses of the CDFs computed in (3.12). This also implies that applying the monotone rearrangement to derivatives of a function results in a different transport map, and this property could be used to construct another monotone rearrangement map. Depending on the context, other maps could be more useful than the solution to the Monge-Kantorovich problem itself.

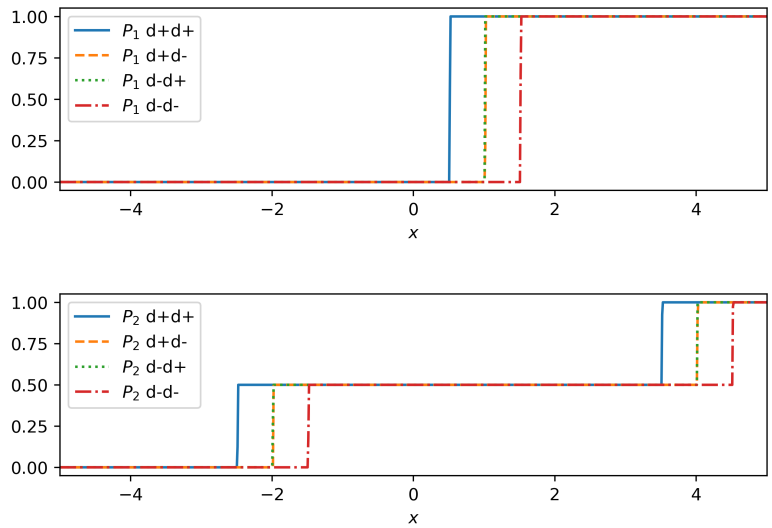

Fig. 14: The CDFs (3.12) of the functions $p_1^{d\pm d\pm}$ (top) and $p_2^{d\pm d\pm}$ (bottom).

.

3.6. 1D Burgers shock. In this example, we consider the interpolation of the sotluion to the 1D Burger's equation,

$$u_t + uu_x = 0. \tag{3.14}$$

As in the previous section, we are interested in the change in the behavior of the solution with respect to the paramter $\alpha = t$, the time variable. Suppose we are given the solution at two times t_1 and t_2, ($u_1 = u(x, t_1)$, $u_2 = u(x, t_2)$) shown in Figure 15(a),(c). The corresponding CDFs (2.8) are shown in Figure 16. The solution u to the Burgers' equation develops shocks, and once a shock is formed, the speed at which the shock travels is determined by the Rankine-Hugoniot jump condition [24]. Although we do not expect the interpolant $\tilde{u}_t$ will agree with the solution u at time t, unlike in the previous example, we aim to recover a reasonable deformation map that will provide a suitable approximation to the evolution of the shock.

The solutions at two different times u_1 and u_2 are shown in the top row of Figure 15. The interpolant $\tilde{u}_t$ where $t = 2$ ($\lambda(t) = 0.5$) is shown in the bottom left plot of the same figure. The dotted line represents the true solution $u(x, t)$. The plot of $\tilde{u}_t$ for 10 different values $t = 1 + 0.2n$ for $n = 1, 2, ..., 10$. is shown in the lower right plot in the same figure. It is easy to see that the speeds of the propagation of the shock is linear with respect to time for the interpolant. This is not true for the true solution, therefore the interpolant is only an approximation whose quality depends on the distance to the nearest data point in the paramter space of $\alpha = t$. However, this yields a far superior approximation than the corresponding linear interpolant of the two.

3.7. 2D displacement interpolation. In this section, we present an example of the interpolant (2.35) with spatial dimension $d = 2$. The two functions $u_1(x, y)$

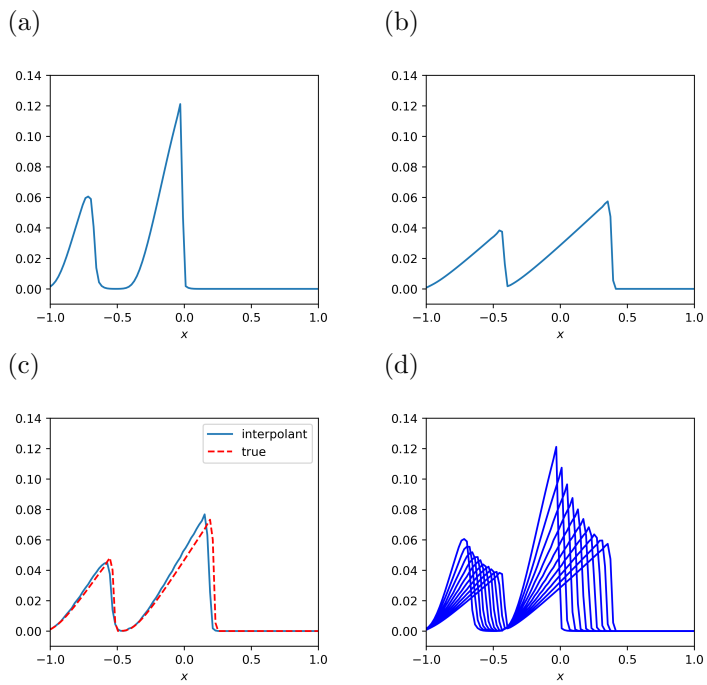

Fig. 15: (a) Solution u to the Burger's equation (3.8) at times $t_1 = 1$ and (b) $t_2 = 3$. (c) Displacement interpolant $\tilde{u}_t$ (3.11) to these two at $t = 2$ or $\lambda(t) = 0.5$, and (d) $\tilde{u}_t$ at times $t = 1 + 0.2n$ for $n = 1, 2, ..., 10$ (bottom right).

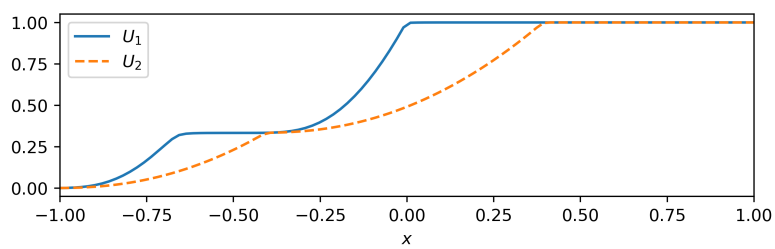

Fig. 16: The cumulative distribution functions (CDFs) of the solution u to the Burger's equation (3.14) at times t_1 and t_2, denoted by U_1 and U_2.

and $u_2(x, y)$ are given as follows,

$$u_1(x, y) = \frac{3}{2} \exp\left[-\frac{(|x| + |y| - 0.75)^2}{2 \cdot (0.2)^2} - \frac{(|x| + |y| - 0.5)^2}{2 \cdot (0.2)^2}\right],$$
$$u_2(x, y) = \frac{3}{2} \exp\left[-\frac{(|x - 0.5| + |y - 0.25|)^2}{2 \cdot (0.05)^2}\right].$$

The first function u_1 is concentrated near a diamond-shaped Gaussian hump centered at the origin, where as u_2 is a much narrower diamond-shaped Gaussian hump centered

at the coordinates $(x, y) = (0.5, 0.25)$. Let us suppose u_1 is the function at parameter $\alpha = 0$ whereas u_2 is a function at parameter $\alpha = 1$.

We compute the interpolant (2.35),

$$\tilde{u}_\alpha = \mathcal{I}_2(\alpha; u_1, u_2) \tag{3.15}$$

for values $\alpha = 0.25, 0.5, 0.75$.

The two functions and the interpolants are shown in Figure 17. The interpolant discovers the translation map, that shifts the center of mass of u_1 towards that of u_2, while shrinking the region of concentrated mass towards the concentrated hump. In the transformed variables (h, s), this transport map is reduced to a 1D monotone rearrangement, and the smooth displacement interpolant we have obtained is a low-dimensional for each slice of the transformed variables for fixed $\boldsymbol{\omega}$. This is clear from (2.33).

3.8. 2D oscillating function. In this example, we will interpolate between 2D oscillatory functions. Let us consider the radial function with a free parameter k,

$$u(r; k) = \exp\left[-\left(\frac{r^2}{2\sigma^2}\right)\right]\cos(k\pi r), \quad \text{where } r = \sqrt{x^2 + y^2}, \quad 0 \le x, y \le 1. \tag{3.16}$$

Let us set σ^2 as 0.0125 and the two functions u_1 and u_2 as

$$u_1(x, y) := u(r; k_1), \quad k_1 = 8 \quad \text{and} \quad u_2(x, y) := u(r; k_2), \quad k_2 = 16. \tag{3.17}$$

We will apply the displacement interpolation of the type $\mathcal{I}_\mathcal{T}$ (2.36) in which we will choose the transform $\mathcal{T}$ as,

$$\mathcal{T} = \mathcal{R} \otimes \mathcal{P}\mathcal{F}, \tag{3.18}$$

where $\mathcal{F}$ is the Fourier transform $\mathcal{P}$ rearranges the Fourier transform,

$$\begin{aligned}\mathcal{P}\mathcal{F}[u] = [&\mathrm{Re}\,(\mathcal{F}[u])_{\mathrm{oo}}, \mathrm{Re}\,(\mathcal{F}[u])_{\mathrm{eo}}, \mathrm{Re}\,(\mathcal{F}[u])_{\mathrm{oe}}, \mathrm{Re}\,(\mathcal{F}[u])_{\mathrm{ee}},\\ &\mathrm{Im}\,(\mathcal{F}[u])_{\mathrm{oo}}, \mathrm{Im}\,(\mathcal{F}[u])_{\mathrm{eo}}, \mathrm{Im}\,(\mathcal{F}[u])_{\mathrm{oe}}, \mathrm{Im}\,(\mathcal{F}[u])_{\mathrm{ee}}]\end{aligned} \tag{3.19}$$

where the subscript indices $\{\mathrm{o}, \mathrm{e}\}$ indicate the restriction to either odd or even sub-indices of the 2D arrays, and $\mathcal{R}\otimes$ acts on the individual components of (3.19). The interpolation $\mathcal{I}_\otimes$ appearing in $\mathcal{I}_\mathcal{T} = \mathcal{T}^{-1}\mathcal{I}_\otimes\mathcal{T}$ acts on the s-variable of the Radon transform, as before.

The functions u_1, u_2 as well as the resulting interpolant $\tilde{u}_\alpha$ with $\alpha = 0.75$, along with the even-even component $\mathrm{Re}\,(\mathcal{F}[\cdot])_{\mathrm{ee}}$ are shown in Figure 18. The interpolant is able to capture the oscillatory nature of the functions (3.16). Note that their Fourier transforms are wave-like and that the location of high amplitudes in the frequency space correspond to the frequency of the oscillation.

Next, let us examine the decay of the singular values of the transport maps computed for different angles of $\mathcal{T}[\cdot]$ for a larger sample of functions of the form (3.16) with more diverse values of k. To be more clear, we consider the SVD of the transport maps between the 1D functions

$$\begin{aligned}\mathcal{T}[v](\cdot, \boldsymbol{\omega}) &= \mathcal{R} \otimes \mathcal{P}\mathcal{F}[v](\cdot, \boldsymbol{\omega})\\ &\quad \text{where } v \in \mathcal{U} := \{u(r; k) : k = 8 + .5j,\ j = 0, 1, ..., 49\}.\end{aligned} \tag{3.20}$$

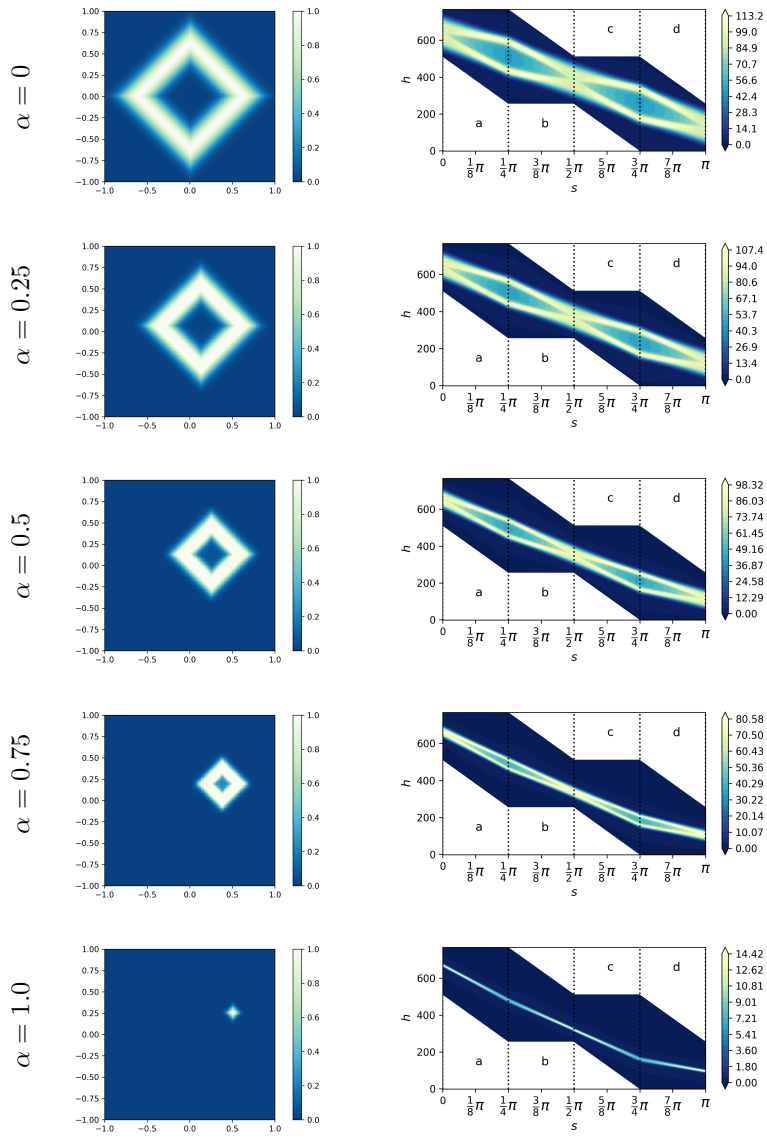

Fig. 17: 2-dimensional displacement interpolant between two functions u_1 and u_2 given in (3.7), shown together with their discrete Radon transform. The functions themselves are given in the first row $\alpha = 0$ and the last row $\alpha = 1$.

We display the sample mean and the standard deviation over all angles $\boldsymbol{\omega}$ of the singular values $s_j(\boldsymbol{\omega})$ computed from these maps in Figure 19, that is,

$$\bar{s}_j := \mathbb{E}_{\boldsymbol{\omega}}\left[s_j(\boldsymbol{\omega})\right] \quad \text{and} \quad \sigma_j := \sqrt{\mathrm{Var}_{\boldsymbol{\omega}}\left[s_j(\boldsymbol{\omega})\right]}. \tag{3.21}$$

There is now a clear decay of singular values, whereas it is straightforward to show that the original functions are nearly orthogonal to each other.

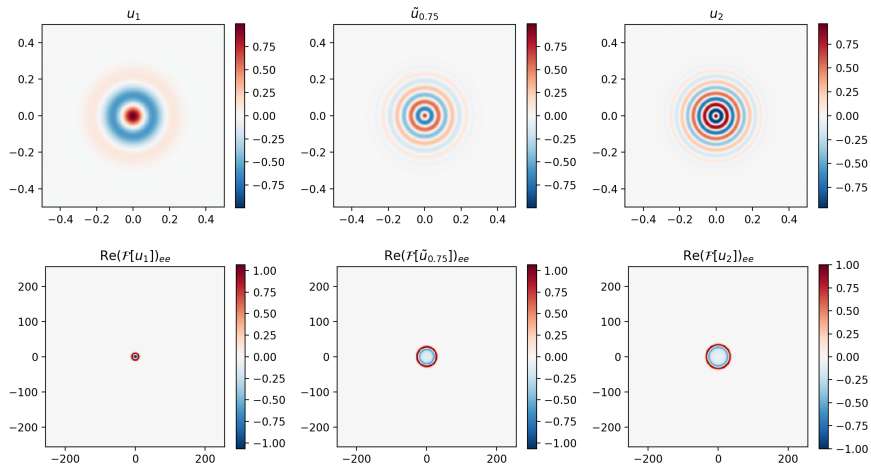

Fig. 18: 2D displacement interpolant between two oscillating functions u_1 and u_2 given in (3.17) and the interpolant $\tilde{u}_{0.75} = \mathcal{I}_{\mathcal{T}}(0.75; u_1, u_2)$ where $\mathcal{T}$ is given by (3.18) (top row), shown together with the corresponding even-even component of $\mathrm{Re}(\mathcal{PF}[u])$ (3.19) (bottom row). The plots have been normalized with respect to the maximum value for ease of comparison.

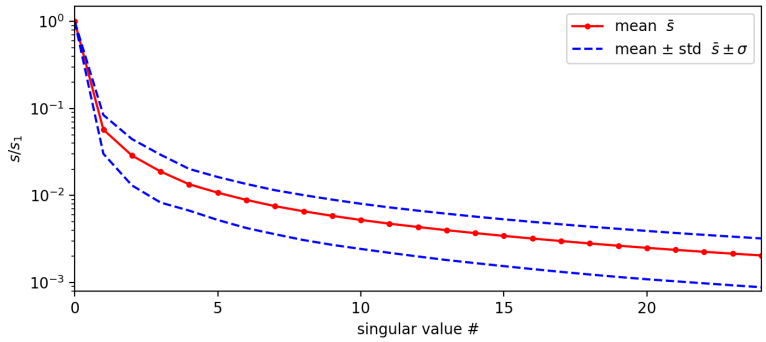

Fig. 19: Mean and standard deviation of the singular values of the transport maps, over all angles $\boldsymbol{\omega} \in S^1$ (3.21).

3.9. Displacement interpolation for oscillatory functions in 2D.

4. Conclusion and future work. We have introduced a displacement interpolation scheme based on monotone rearrangement solution to the Monge-Kantorovich problem in 1D. We extended this to the case when the given functions have arbitrary sign, as well as when multiple functions are given. We then showed that this scheme can be naturally generalized to multiple spatial dimensions through the use of the Radon transform, resulting in a generalization of the Lax-Philips transform.

The interpolation allowed the authors to achieve the dimensionality reduction of wave-like phenomena in 1D scalar conservation laws [38], and we will investiage its

application in the model reduction of hyperbolic PDEs in a multi-dimensional setting in a future work. The interpolation method is by no means restricted to hyperbolic PDEs, however, and may well complement existing dimensionality reduction methods in various applications where standard methods are unsuccessful.

REFERENCES

[1] R. Abgrall and D. Amsallem, *Robust model reduction by L^1-norm minimization and approximation via dictionaries: Application to linear and nonlinear hyperbolic problems*, Advanced Modeling and Simulation in Engineering Sciences, 3 (2016), p. 1.

[2] M. Agueh and G. Carlier, *Barycenters in the Wasserstein space*, SIAM Journal on Mathematical Analysis, 43 (2011), pp. 904–924.

[3] J. Benamou, G. Carlier, M. Cuturi, L. Nenna, and G. Peyré, *Iterative Bregman projections for regularized transportation problems*, SIAM Journal on Scientific Computing, 37 (2015), pp. A1111–A1138.

[4] J.-D. Benamou and Y. Brenier, *A computational fluid mechanics solution to the monge-kantorovich mass transfer problem*, Numerische Mathematik, 84 (2000), pp. 375–393.

[5] F. Bolley, Y. Brenier, and G. Loeper, *Contractive metrics for scalar conservation laws*, Journal of Hyperbolic Differential Equations, 02 (2005), pp. 91–107.

[6] N. Bonneel, J. Rabin, G. Peyré, and H. Pfister, *Sliced and Radon Wasserstein barycenters of measures*, Journal of Mathematical Imaging and Vision, 51 (2015), pp. 22–45.

[7] N. Bonneel, M. van de Panne, S. Paris, and W. Heidrich, *Displacement interpolation using lagrangian mass transport*, ACM Trans. Graph., 30 (2011), pp. 158:1–158:12.

[8] M. L. Brady, *A fast discrete approximation algorithm for the Radon transform*, SIAM Journal on Computing, 27 (1998), pp. 107–119.

[9] M. Cuturi, *Sinkhorn distances: Lightspeed computation of optimal transport*, in Advances in Neural Information Processing Systems 26, C. J. C. Burges, L. Bottou, M. Welling, Z. Ghahramani, and K. Q. Weinberger, eds., Curran Associates, Inc., 2013, pp. 2292–2300.

[10] I. Daubechies, *Ten Lectures on Wavelets*, Society for Industrial and Applied Mathematics, 1992.

[11] T. de Wet, *Goodnes-of-fit tests for location and scale families based on a weighted L_2-Wasserstein distance measure*, Test, 11 (2002), pp. 89–107.

[12] E. del Barrio, J. A. Cuesta-Albertos, C. Matran, and J. M. Rodriguez-Rodriguez, *Tests of goodness of fit based on the L_2-Wasserstein distance*, The Annals of Statistics, 27 (1999), pp. 1230–1239.

[13] J. Delon, *Midway image equalization*, Journal of Mathematical Imaging and Vision, 21 (2004), pp. 119–134.

[14] R. Dobrushin, *Prescribing a system of random variables by conditional distributions*, Theory of Probability & Its Applications, 15 (1970), pp. 458–486.

[15] B. Engquist and H. Zhao, *Approximate separability of the Green's function of the Helmholtz equation in the high frequency limit*, Communications on Pure and Applied Mathematics, 0.

[16] C. Frogner, C. Zhang, H. Mobahi, M. Araya, and T. A. Poggio, *Learning with a Wasserstein loss*, in Advances in Neural Information Processing Systems 28, C. Cortes, N. D. Lawrence, D. D. Lee, M. Sugiyama, and R. Garnett, eds., Curran Associates, Inc., 2015, pp. 2053–2061.

[17] W. Gangbo and R. J. McCann, *The geometry of optimal transportation*, Acta Mathematica, 177 (1996), pp. 113–161.

[18] A. Greenbaum, *Iterative Methods for Solving Linear Systems*, Society for Industrial and Applied Mathematics, 1997.

[19] S. Helgason, *Integral Geometry and Radon Transforms*, Springer New York, New York, NY, 2011.

[20] J. S. Hesthaven, G. Rozza, and B. Stamm, Springer Cham, Cham, Switzerland, 2016.

[21] A. Iollo and D. Lombardi, *Advection modes by optimal mass transfer*, Phys. Rev. E, 89 (2014), p. 022923.

[22] L. V. Kantorovich, *On a problem of Monge*, Uspekhi Mat. Nauk, 3 (1948), pp. 225–226.

[23] P. D. Lax and R. S. Phillips, *Scattering theory*, Bull. Amer. Math. Soc., 70 (1964), pp. 130–142.

[24] R. J. LeVeque, *Finite Volume Methods for Hyperbolic Problems*, Cambridge University Press, Cambridge, 1st ed., 2002.

[25] C. L. Mallows, *A note on asymptotic joint normality*, The Annals of Mathematical Statistics,

43 (1972), pp. 508–515.

[26] R. J. McCann, *A convexity principle for interacting gases*, Advances in Mathematics, 128 (1997), pp. 153 – 179.

[27] A. Munk and C. Czado, *Nonparametric validation of similar distributions and assessment of goodness of fit*, Journal of the Royal Statistical Society: Series B (Statistical Methodology), 60, pp. 223–241.

[28] L. Métivier, R. Brossier, Q. Mérigot, E. Oudet, and J. Virieux, *An optimal transport approach for seismic tomography: application to 3d full waveform inversion*, Inverse Problems, 32 (2016), p. 115008.

[29] F. Natterer, *The Mathematics of Computerized Tomography*, Society for Industrial and Applied Mathematics, 2001.

[30] S. G. P. Benner and K. Willcox, *A survey of projection-based model reduction methods for parametric dynamical systems*, SIAM Rev., 57 (2015), pp. 483–531.

[31] F. Pitié, A. C. Kokaram, and R. Dahyot, *Automated colour grading using colour distribution transfer*, Computer Vision and Image Understanding, 107 (2007), pp. 123 – 137.

[32] W. H. Press, *Discrete Radon transform has an exact, fast inverse and generalizes to operations other than sums along lines*, Proceedings of the National Academy of Sciences, 103 (2006), pp. 19249–19254.

[33] J. Rabin, G. Peyré, J. Delon, and M. Bernot, *Wasserstein barycenter and its application to texture mixing*, in Scale Space and Variational Methods in Computer Vision, A. M. Bruckstein, B. M. ter Haar Romeny, A. M. Bronstein, and M. M. Bronstein, eds., Berlin, Heidelberg, 2012, Springer Berlin Heidelberg, pp. 435–446.

[34] J. Reiss, P. Schulze, J. Sesterhenn, and V. Mehrmann, *The shifted proper orthogonal decomposition: A mode decomposition for multiple transport phenomena*, (2015), arXiv:1512.01985.

[35] D. Rim, *Dimensional splitting of hyperbolic partial differential equations using the Radon transform*, (2017), arXiv:1705.03609.

[36] D. Rim, *Uncertainty quantification problems in tsunami modeling and reduced order models for hyperbolic partial differential equations*, Ph.D. Thesis, University of Washington, (2017).

[37] D. Rim, *Code archive*, 2018. doi:10.5281/zenodo.1405576.

[38] D. Rim and K. Mandli, *Model reduction of a parametrized scalar hyperbolic conservation law using displacement interpolation*, Preprint, (2018), arXiv:1805.05938.

[39] D. Rim, S. Moe, and R. LeVeque, *Transport reversal for model reduction of hyperbolic partial differential equations*, SIAM/ASA Journal on Uncertainty Quantification, 6 (2018), pp. 118–150.

[40] C. W. Rowley and J. E. Marsden, *Reconstruction equations and the Karhunen-Loève expansion for systems with symmetry*, Physica D, (2000), pp. 1–19.

[41] J. Solomon, F. de Goes, G. Peyré, M. Cuturi, A. Butscher, A. Nguyen, T. Du, and L. Guibas, *Convolutional Wasserstein distances: Efficient optimal transportation on geometric domains*, ACM Trans. Graph., 34 (2015), pp. 66:1–66:11.

[42] G. Szegö, *Orthogonal Polynomials*, American Mathematical Society, New York, NY, USA, 1939.

[43] L. N. Trefethen, *Approximation Theory and Approximation Practice*, Society for Industrial and Applied Mathematics, Philadelphia, PA, USA, 2012.

[44] C. Villani, *Topics in Optimal Transportation*, American Mathematical Society, Providence, RI, 2003.

[45] C. Villani, *Optimal transport: old and new*, vol. 338, Springer Science & Business Media, 2008.

[46] G. Welper, *h and hp-adaptive Interpolation by Transformed Snapshots for Parametric and Stochastic Hyperbolic PDEs*, `arXiv:1710.11481 [math.NA]` (2017), arXiv:1710.11481.

[47] G. Welper, *Interpolation of functions with parameter dependent jumps by transformed snapshots*, SIAM Journal on Scientific Computing, 39 (2017), pp. A1225–A1250.

[48] D. Xiu, *Numerical Methods for Stochastic Computations: A Spectral Method Approach*, Princeton University Press, Princeton, NJ, USA, 2010.

[49] Y. Yang, B. Engquist, J. Sun, and B. F. Hamfeldt, *Application of optimal transport and the quadratic Wasserstein metric to full-waveform inversion*, Geophysics, 83 (2018), pp. R43–R62.

[50] A. Zygmund and R. Fefferman, *Trigonometric Series*, Cambridge Mathematical Library, Cambridge University Press, 3 ed., 2003.